

Exploring Water Accumulation Dynamics in the Pearl River Estuary from a Lagrangian Perspective

Mingyu Li¹, Alessandro Stocchino^{2,3}, Zhongya Cai^{1,3}, Tingting Zu⁴

¹State Key Laboratory of Internet of Thing for Smart City, Department of Ocean Science and Technology, University of Macau, Macau, 999078, China

²Department of Civil and Environmental Engineering, The Hong Kong Polytechnic University, Hong Kong, 999077, China

³Center for Ocean Research in Hong Kong and Macau (CORE), Hong Kong, 999077, China

⁴State Key Laboratory of Tropical Oceanography, South China Sea Institute of Oceanology, Chinese Academy of Sciences, Guangzhou, 510301, China

10 *Correspondence to:* Zhongya Cai (zyc@um.edu.mo); Tingting Zu (zutt@scsio.ac.cn)

Abstract. Water accumulation is essential for understanding estuarine mass distribution and ecosystem management. In this study, we examined the water accumulation dynamics in the Pearl River Estuary (PRE) from a Lagrangian perspective. Generally, there is a notable negative correlation between the horizontal velocity divergence ($\nabla_h \cdot \vec{V}_h$) and the accumulation. Influenced by density fronts and velocity convergence, we observed significant bottom-layer accumulation of particles in the western estuary and Hong Kong waters during summer, whereas the accumulation moved landward in winter. Sub-regions with distinct accumulation patterns and interconnections were identified and combined with the trajectories. In summer, the western estuary and Macau waters have a substantial net negative $\nabla_h \cdot \vec{V}_h$ and strong density fronts are major accumulation targets, which attract particles from the whole estuary. Conversely, the eastern estuary and Hong Kong waters exhibit significant westward motion, influencing the western side. In winter, particles are more likely to accumulate in their original locations. The upper estuary becomes a major accumulation area because of the obstructive density front, and decreased river discharges. The tidal currents and river discharges mainly control water accumulation in the estuary by changing the mixing or current intensity. The weakening of tidal currents and river discharges induced the intensified bottom intrusion and the landward movement of accumulation.

25 1 Introduction

The Pearl River Estuary (PRE), located in the northern South China Sea (NSCS) (Fig. 1a), is influenced by the East Asian Monsoon, with northeasterly winds prevailing in winter and southwesterly winds prevailing in summer (Li & Li, 2018). Thus, in the PRE, winter is characterized as a dry season, and summer is characterized as a wet season due to the large rainfall induced by the moist air brought from the South China Sea; consequently, the river discharge in summer (~ 20,000 m³s⁻¹) is approximately five times more than that in winter (~ 3,600 m³s⁻¹) (Harrison, Yin, Lee, Gan, & Liu, 2008). This is quite different from many other river deltas, such as the Mississippi deltas, where river discharge reaches a maximum in winter and spring, but is reduced in summer and autumn (Lane et al., 2007).

As a bell-shaped estuary, the width increases from approximately 5 km at the upper end to 35 km at the lower end. Despite the two narrow, deeper channels (~20 m in depth), the PRE is shallow, with a water depth of approximately 2-10 m. **The PRE is a partially-mixed estuary in which circulation is jointly controlled by river discharge, tides, wind, and topography** (Ascione Kenov, Garcia, & Neves, 2012; Banas & Hickey, 2005; Gong, Shen, & Hong, 2009; He, Yin, Stocchino, & Wai, 2023; He, Yin, Stocchino, Wai, & Li, 2022; Liu, Zu, & Gan, 2020). There are two distinct dynamic regimes in the PRE. The narrow upper part of the PRE shows classical gravitational circulation, whereas in the wider lower part of the PRE, where the Coriolis effect becomes essential, the topography and interaction with the monsoon-driven shelf current complicate the circulation (Dong, Su, Ah Wong, Cao, & Chen, 2004; Wong et al., 2003; Zu & Gan, 2015). Gravitational circulation occurs in the two deep channel regions, whereas currents show precise seasonal characteristics over the shallower western estuary. Geostrophic wind-driven coastal currents intrude into the PRE during the summer upwelling season (Zu & Gan, 2015), whereas seaward buoyancy-driven coastal currents flow out of the PRE during winter (Dong et al., 2004; Wong et al., 2003). The alternation of the spring-neap tide and variation in river discharge play crucial roles in modulating stratification and mixing inside the PRE (Mao, Shi, Yin, Gan, & Qi, 2004; Pan, Lai, & Thomas Devlin, 2020; Zu, Wang, Gan, & Guan, 2014). Strong tidal mixing in the middle PRE has led to the conversion of estuarine river plumes into buoyancy-driven coastal currents (Dong et al., 2004; Zu et al., 2014).

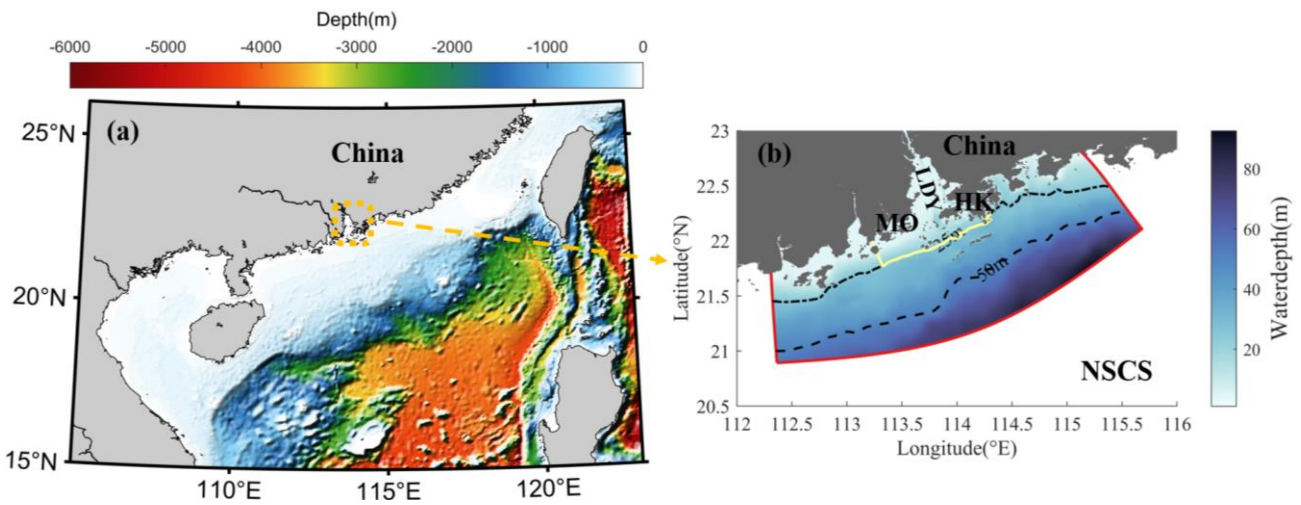
In recent decades, the state and sustainability of estuaries have been increasingly imperiled by environmental issues caused by anthropogenic activities and climate variability (Dai et al., 2006; Fok & Cheung, 2015; Shen, Wei, Shi, Gao, & Zhou, 2023). Estuarine circulation and the associated mass transport are critical for addressing these environmental challenges. **The specific areas of water accumulation and the extent of its exchange with the open sea significantly impact the dispersion of oceanic pollutants and biogeochemical conditions** (Acha, Mianzan, Guerrero, Favero, & Bava, 2004; Hinojosa, Rivadeneira, & Thiel, 2011). In estuaries, some regions are more likely to attract water because of complicated current

circulation, which can be considered as stronger horizontal convergence targets for some materials (Wang et al., 2022).
55 For example, the salt wedge acts as a significant pollutant sink in an estuary, with higher concentrations of microplastics
consistently found at the salt wedge in the Rio de la Plata estuary (Acha et al., 2003; Vermeiren, Muñoz, & Ikejima, 2016).
Areas accompanied with higher concentration of nitrogen and phosphorus are usually appear eutrophic (Tao, Niu, Dong,
Fu, & Lou, 2021). Heavy metal pollution in estuaries has been observed in areas that prefer to concentrate fine particles
(Balachandran et al., 2005). Therefore, identifying the accumulation areas in estuary-shelf systems is crucial for accurately
60 surveying pollutant sinks (Mestres et al., 2006; Tao et al., 2021; Vermeiren et al., 2016; Wang et al., 2016).

With intensified human activities, pollutant sinks related to the accumulation phenomena in the PRE have garnered
attention. Tao et al. (2021) revealed that the upper part of the PRE as a key sink for nitrogen and silicate. Zhang et al. (2013)
found that trace elements prefer to accumulate on the PRE's west side. Higher concentrations of microplastics have been
observed in western estuaries and Hong Kong waters (Lam et al., 2020). Similarly, studies on hypoxia have shown that the
65 convergence of buoyancy-driven currents and wind-driven shelf flows contributes to the formation of stable water columns,
creating favorable conditions for the development of hypoxic zones (e.g., Li et al. (2021); Li et al. (2020)). The high
frequency of hypoxia in the estuary during summer is linked to the strong stratification of the water column (Cui, Wu, Ren,
& Xu, 2019; Zhang & Li, 2010). These accumulation patterns in the PRE focus more on measuring pollutant concentrations
(Tao et al., 2021), estimating pollutant accumulation rate (Zhang et al., 2009), and discussing pollutant sources (Ye, Huang,
70 Zhang, Tian, & Zeng, 2012), but lack a comprehensive understanding of the spatial accumulation patterns and the
underlying physical controls.

The Lagrangian tracking method provides an effective way to analyze the transport processes in physical
oceanography (Jalón-Rojas, Wang, & Fredj, 2019; van Sebille et al., 2018). It involves analyzing the sizeable virtual particle
trajectories calculated from simulated Eulerian three-dimensional and time-varying velocity fields, which capture complex
75 real-world dynamical processes. Their applications extend across various domains, including interocean exchange (Haza,
Özgökmen, & Hogan, 2016), pathway analysis (Jalón-Rojas et al., 2019), and the impact of ocean currents on ecosystems
(Chenillat et al., 2015; Dawson, Sen Gupta, & England, 2005; Lebreton, Greer, & Borrero, 2012; Paris et al., 2012).

In this study, Lagrangian tracking and analysis were utilized to examine the features of the accumulation regions in the
estuary-shelf system of the PRE and to explore the role of various forcing factors. These results enhance our understanding
80 of the environmental effects of multi-scale processes. The remainder of this paper is organized as follows. Section 2
introduces the Lagrangian model and numerical solutions of the Markov Chain. Findings regarding the accumulation region
and transport connections in the PRE are discussed in Sect. 3. Section 4 presents the roles of hydrodynamic factors. Finally,
Section 5 presents the conclusions of this study.



85 **Figure 1: (a) Location and topography of the Pearl River Estuary (PRE) and adjacent shelf. (b) The bathymetry of the PRE and adjacent shelf. The black dotted and dashed lines represent the 25 m and 50 m isobath. The yellow line defines the seaside boundary of the PRE. LDY, MO, HK and NSCS represent Lingdingyang, Macau, Hong Kong and northern South China Sea, respectively. The red line represents the model boundary.**

90

2 Methods

2.1 Numerical simulation and Lagrangian particle tracking

In this study, multi-scale circulation in the PRE and adjacent shelf regions was simulated by implementing the Regional Ocean Modeling System (Shchepetkin & McWilliams, 2005). The model region covers the estuary and adjacent shelf
 95 between 112.3°E-115.68°E and 20.89°N-23.13°N (Fig. 1b). An orthogonal curvilinear grid was employed, with resolution increasing gradually from approximately 1 km over the shelf to ~ 200 m inside the estuary. In the vertical direction, we used the terrain-following S-ordinate (Song & Haidvogel, 1994) to discretize the water column into 30 layers.

The monthly average riverine discharge data were obtained from the Ministry of Water Resources of China. River discharge was approximately 30000 m³/s and 10000 m³/s in summer and winter (Fig. S1), respectively. Wind forcing, heat flux, and
 100 precipitation were obtained from ERA5 atmospheric reanalysis data from the European Center for Medium-Range Weather Forecasts (ECMWF) and were used to force ocean circulation through the implementation of the bulk computation algorithm (Fairall, Bradley, Hare, Grachev, & Edson, 2003). The shelf current was obtained from a coarser model with good validation that can cover the NSCS (Fig. S2), providing information on the barotropic and baroclinic velocities, temperature, salinity, and sea level along the boundaries of the PRE (Deng et al., 2022). Vertical turbulence and diffusion

105 coefficient are determined using the Mellor-Yamada 2.5 turbulence-closure module (Mellor & Yamada, 1982), which

provides the turbulent mixing coefficient. Tidal current simulations, considering forcing along open boundaries were obtained from Zu, Gan, and Erofeeva (2008), including the tidal harmonic constants (M_2 , S_2 , K_2 , N_2 , K_1 , O_1 , P_1 , Q_1 , and M_4). This model, based primarily on climatological data, was carefully verified using satellite remote sensing and long-term observations to ensure an accurate representation of the hydrodynamic properties (Fig. S3, 4). Overall, the model accurately captured the seasonal variability of the hydrodynamic features in this region and has been used in previous studies (Cai, Liu, Liu, & Gan, 2022; Chu et al., 2022b; Cui, Liu, Chen, & Cai, 2024).

Particle trajectories were traced using a three-dimensional offline Lagrangian TRANSport model (LTRANS v.2b), which captures complicated dynamical processes in the real world through Eulerian flow fields and turbulent mixing from the hydrodynamic model (Chu et al., 2022a; Liang et al., 2021; North et al., 2011). To reasonably calculate the Lagrangian trajectories within the estuary-shelf circulation systems, the tracking model considers the advection, turbulence, individual behaviors of particles (e.g., vertical sinking, floating, or swimming velocity), settlement, and boundary behaviors during particle trajectory simulations. The 4th order Runge-Kutta scheme was implemented to handle the advective terms and yield accurate particle trajectories (Dippner, 2009). Considering the random walk of water parcels in the ocean, the model adopts different diffusivity coefficients to control the vertical and horizontal turbulence (North, Hood, Chao, & Sanford, 2006; Zhong & Li, 2006). In the surface/bottom tracking case, 8386 particles were uniformly distributed at water surface/bottom across the estuary and adjacent shelf with a 0.01 degree interval. Particles were released every two days and tracked for 20 days. The hydrodynamic simulation results were stored every 20 min in January and July to drive the particle tracking during summer and winter, respectively. During trajectory tracking, the time step of particle tracking was 30 seconds, and their locations were recorded every 20 minutes.

2.2 Markov Chain

In this study, to investigate the accumulation features and connectivity among different parts of the domain, we implement the Markov Chains statistical analysis to describe the future state of a random variable, which is based on the particle's original state positions, allowing us to compute a proper transition matrix (Drouin & Lozier, 2019; Drouin, Lozier, Beron-Vera, Miron, & Olascoaga, 2022; Miron, Beron-Vera, Helfmann, & Koltai, 2021; Miron et al., 2019; Miron et al., 2017; van Sebille et al., 2018). To this end, we divided the study area into rectangular grids with dimensions of 0.1 degree, and then the probability of particles moving between different grids within the time interval of dt was calculated as

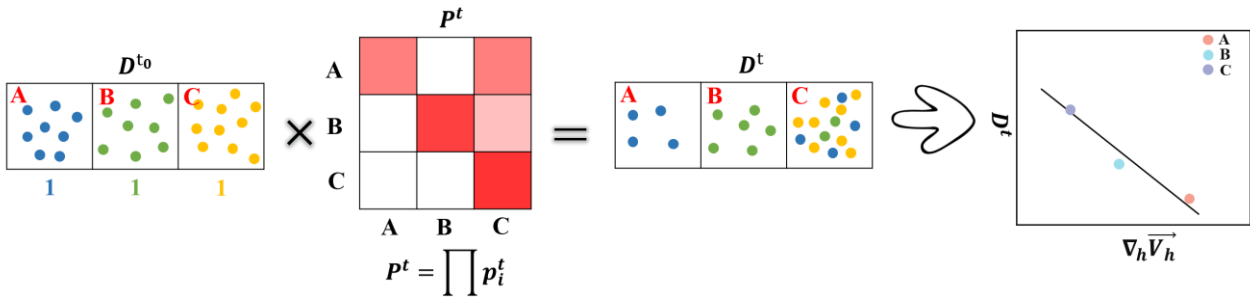
$$p^t = \frac{n_{ij}^{t_0+dt}}{n_i^{t_0}}, \quad (1)$$

where $n_i^{t_0}$ represents the number of particles released in grid i at initial time t . $n_{ij}^{t_0+dt}$ represents the number of particles

arriving at grid j from grid i after interval time dt . Thus, p^t varies for different release grids i , arrival grids j and periods
 135 $(t_0, t_0 + dt)$. Then, the evolution of the initial distribution (D^{t_0}) into a future state (D^{t_0+dt}) is achieved by vector-matrix
 multiplication:

$$D^t = D^{t_0} \times \prod p^t, \quad (2)$$

In this study, the D^{t_0} is defined as a uniform initial mass distribution in the whole domain that $D^{t_0} = [1, 1, 1, \dots, 1]$. The D^t
 is the evolution of the initial condition under complicated hydrodynamic motion, which calculated from the multiplication
 140 of the D^{t_0} with the transition matrix P^t (Fig. 2). The transition matrix P^t is derived from the multiplication of the
 probability matrix p^t , illustrate the net probability trend between different regions in the study area. Areas with high values
 in D^t act as strong accumulation targets of particles.



145 **Figure 2: The schematic in the calculation of the Markov Chains.**

The transport matrix generated by Markov Chains aids in predicting longer timescale transport pathways through limited
 short-time trajectories and is widely used to explore transport pathways and the connectivity of water parcels between
 different regions. For instance, van Sebille et al. (2018) investigated the pathways of significant currents in the Agulhas
 150 Current, while Drouin et al. (2022) found that Caribbean and Gulf of Mexico did not involve the water transition between
 North Brazil Current and 26°N effectively. Studies by Jönsson and Watson (2016) and Drouin et al. (2022) have shown
 that the choice of dt does not significantly influence the results of transport patterns. For the present analysis, we selected
 a time interval (dt) of 2 days.

155 **3 Results**

3.1 Accumulation pattern and regional connectivity

We set up a standard real-world case to explore the accumulation pattern and regional connectivity, considering river discharge, tidal currents, and wind forcing. Before examining the detailed transport structure, we examined the offshore transport speed of particles after their release. Using all the particle trajectories, Figure 3 shows the percentage of particles remaining inside the PRE during summer and winter. Here, the seaside boundary of the PRE is defined by a 25 m isobath (yellow line in Fig. 1). If particles move beyond the seaside boundary of the estuary, they may return to the study area due to tidal currents and wind forcing. However, once particles reach the model domain, they will not be backed again. Overall, the decay speed is faster in summer than in winter, with offshore motions at the surface layer always being quicker than at the bottom layer. Using a value of 20% as a threshold (green dotted line in Fig. 3), during summer, approximately 80% of the surface particles exit the estuary in approximately 10 days, whereas the bottom particles take around 15 days. In contrast, during the winter season, with reduced river discharge, the exit time increases to 20 days (for the surface particles) and 25 days (for the bottom particles). Thus, for the entire domain, after being tracked for 20 days, most particles leave the seaside boundary, and their trajectories are used in the following analysis. **Using the trajectories of the released particles within 20 days, we explored the final evolved state to quantify the accumulation targets resulting from the complex hydrodynamics of estuarine circulation.**

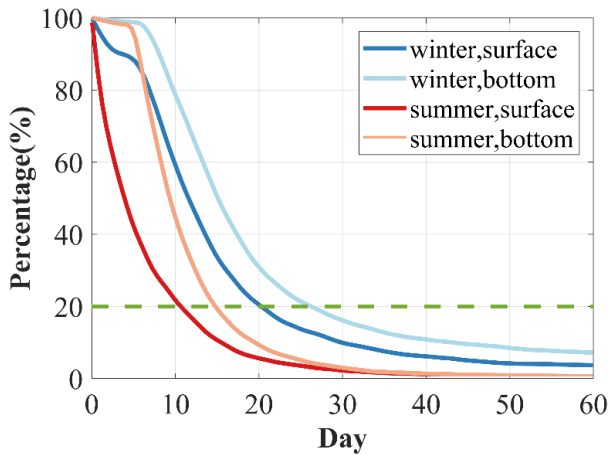


Figure 3: The changes of particle percentage remaining in the estuary during tracking.

According to the circulation in the standard case (Fig. S5), intensified offshore motions are consistently observed at the surface layer in both summer and winter. Owing to the reduction in river discharge, the offshore current in the upper estuary is weaker during winter than during summer. The shelf current intrudes into the estuary from the west side of Hong Kong and arrives at the middle estuary at the bottom, with this bottom intrusion being more pronounced in winter. We select the AB transect along the intrusion channel (Fig. S5b) to further examine the density stratification and vertical circulation (Fig.

180 4e, f). A large amount of river discharge in summer pushes fresh water to the seaside, resulting in the seaward movement of seawater (indicated by the isopycnal line of $1015 \text{ kg}\cdot\text{m}^{-3}$). In winter, the decreased river discharge caused weaker resistance abilities of fresh water to hinder the intrusion of saltwater.

Figure 4 shows the D^t , in which regions of high value represent the favorable targets for particles accumulation. As a result, compared to the bottom layer, because of the strong offshore current in the surface layer, the surface particles tend to escape
185 from the estuary quickly, resulting in a very low accumulation (Fig. 4a, c). On the contrary, at the bottom layer (Fig. 4b, d), the accumulation targets are much more apparent. In summer, high accumulations are observed on the western and southwestern sides (near Macau) and in Hong Kong waters, which are associated with the westward transport current of Hong Kong water and the intensified intrusion current in the lower estuary. Although these regions are close to the open shelf, they are primary accumulation zones that capture particles initially released in other areas of the domain. Cruise
190 observation data (2014-2018) also indicates that these regions generally have a high frequency of hypoxia under the accumulation effect of hydrodynamic processes (Li et al., 2021).

During winter, with fewer river discharges, gravitational circulation is generally preserved but with weakened intensity. The accumulation regions move shoreward, particularly in the upper estuary, due to the decreased circulation and landward movement of the dense intrusions. Owing to the intensified northeasterly wind, the westward transport of Hong Kong water
195 and the adjacent shelf current are strengthened, leading to higher accumulations along the west side of the estuary.

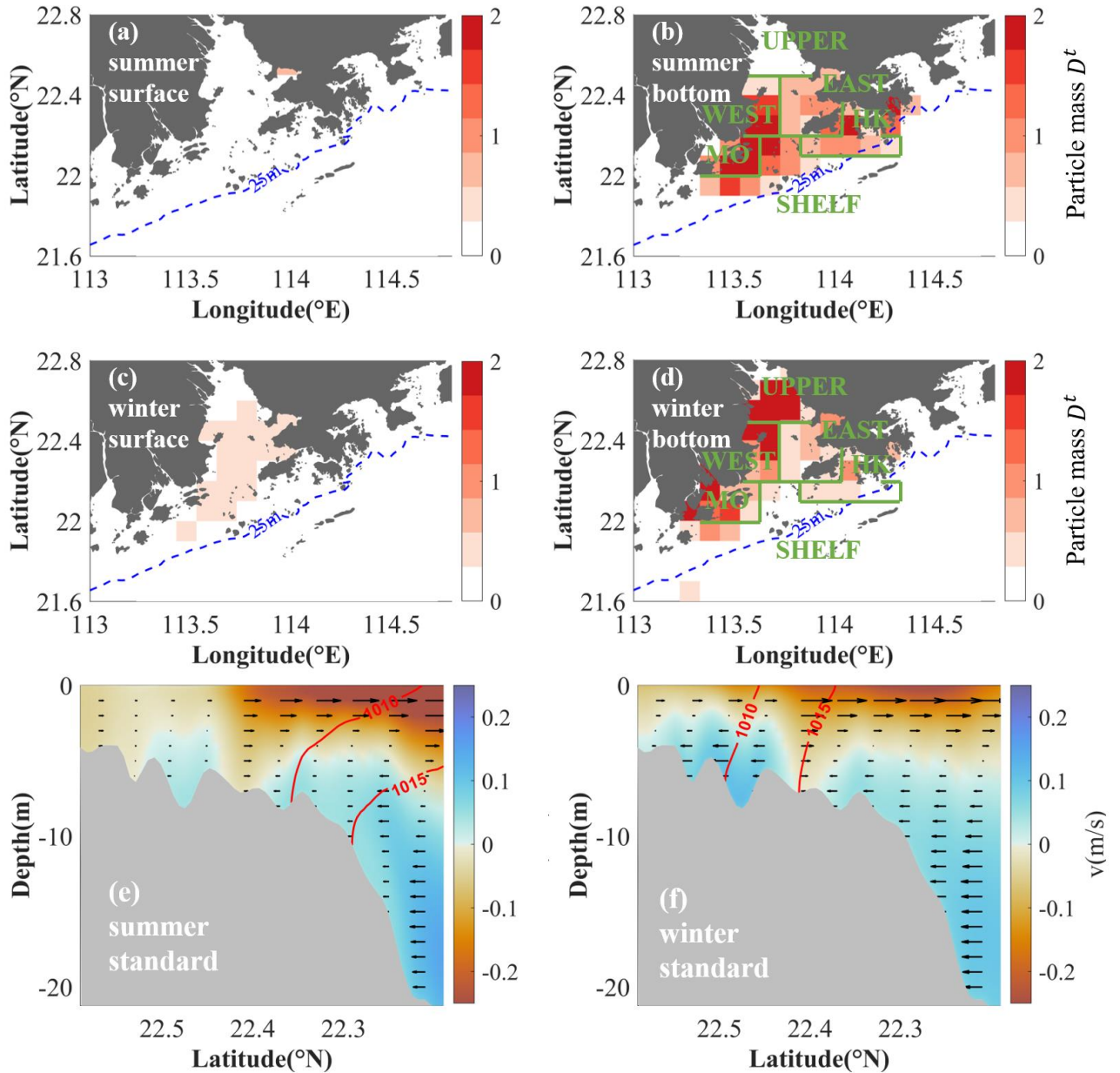


Figure 4: (a–b) Particle mass (color, D^t) at the surface layer and bottom layer during summer time, respectively. Higher value represents stronger accumulation. (c–d) is the same as (a–b) but during winter time. (e–f) The along transect velocity (color and arrows, a positive value indicates the onshore intrusion) and density contour of $1010 \text{ kg}\cdot\text{m}^{-3}$ and $1015 \text{ kg}\cdot\text{m}^{-3}$ (red lines) in AB during summer and winter time, respectively. The location of AB is shown in Fig. S5b.

200

Compared to the bottom layer, the quicker motion at the surface layer cannot distinctly reveal an accumulation pattern. Hence, the accumulation pattern and regional connectivity are focused on the bottom layer. Based on the bottom accumulation patterns (Fig. 4b, d), the study area is divided into six subregions: the Upper Estuary (UPPER), Western Estuary (WEST), Eastern Estuary (EAST), Hong Kong Water (HK), Macau Water (MO), and Shelf Water (SHELF). Subsequently, using the trajectories, the transition matrix (P^t) among each region during the tracking period is examined

205

(Fig. 5). Sensitivity experiments show that different tracking periods do not significantly change the significant patterns of the transition matrix.

During summer (Fig. 5a), the original region consistently contributes significantly to particles accumulation. For the WEST and MO regions, which exhibit the most significant attraction ability, accumulates water from almost all subregions, including the shelf. The onshore intrusion from the shelf water, offshore motions from the upper estuary due to river discharge, and westward transport from EAST and HK converge water in WEST and MO, facilitating particle accumulation in these regions. In contrast, the EAST and HK regions accumulate particles mainly from the eastern side of the estuary. Despite the Eulerian currents, there is an onshore intrusion from the shelf and offshore transport from the upper estuary toward these areas.

During winter, accumulation regions move shoreward and mainly occur in the UPPER, WEST, and MO regions (Fig. 5b). The particles accumulated in those regions are mainly from the original release regions; making it more challenging for the water to leave the original regions. HK water can affect almost the entire estuary, particularly contributing to arrival targets in the WEST region.

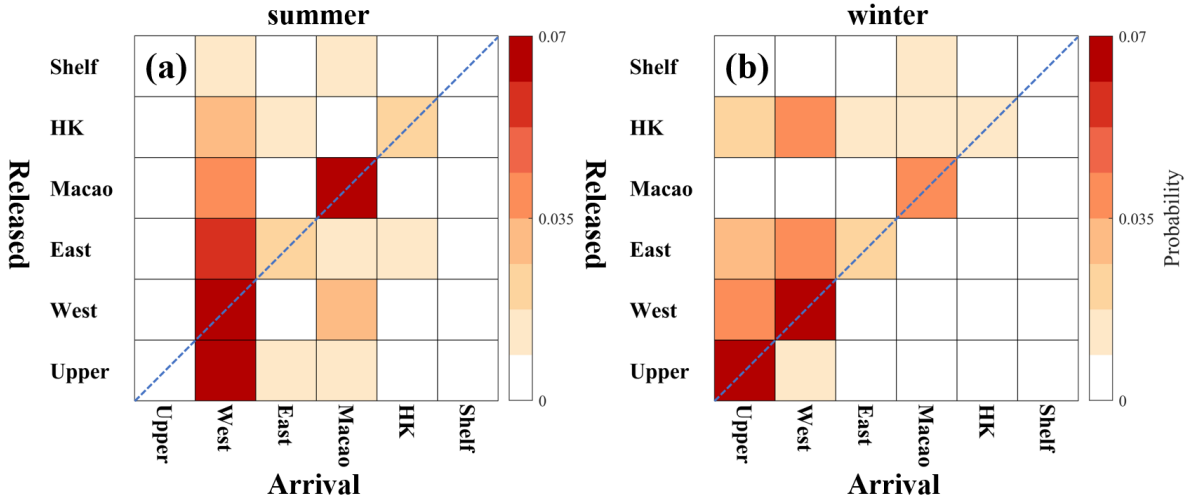


Figure 5: The connection between six subregions at the bottom layer during the summer (a) and winter (b). The horizontal and vertical axes represented the arrival and release regions, respectively.

225 3.2 Hydrodynamic Control on the Accumulation

The bottom divergence of the horizontal current, i.e., $\nabla_h \cdot \vec{V}_h = \frac{\partial u}{\partial x} + \frac{\partial v}{\partial y}$, which u and v represent the bottom zonal and meridional velocity, is calculated to examine its influence on the identified bottom accumulation regions (Fig. 6a, b). We established a connection between the average D^t in each subregion and the divergence of the horizontal current $\nabla_h \cdot \vec{V}_h$.

Across the various identified subregions, a substantial negative correlation between $\nabla_h \cdot \vec{V}_h$ and the particle mass is observed, with correlation coefficients of 0.74 in summer and 0.76 in winter. This suggests that the net negative $\nabla_h \cdot \vec{V}_h$, i.e., the convergence of the water provides a favorable condition for the accumulation of water and particles. Such patterns are noted in major accumulation regions, such as the WEST, MO, and UPPER regions, during both summer and winter. It is also noted that the EAST and HK regions, which show the accumulation of particles, exhibit a weak net positive value of $\nabla_h \cdot \vec{V}_h$. This implies that $\nabla_h \cdot \vec{V}_h$ facilitates accumulation under certain conditions, but actual net accumulation should consider the cumulative effects of velocity convergence along the trajectories, which stay at different locations during the movement. The spatial distribution of $\nabla_h \cdot \vec{V}_h$ also illustrates that intensified negative values occurring in regions with high particle mass (Fig. 6c-d), such as the substantial negative $\nabla_h \cdot \vec{V}_h$ observed in MO and WEST regions during summer, as well as in the UPPER region and central part of the HK region during winter. However, the Eulerian perspective of $\nabla_h \cdot \vec{V}_h$ presents a complex distribution of alternative positive and negative values, which does not straightforwardly identify net accumulation areas. Instead, Lagrangian tracking offers a clearer understanding of these regions because it captures the cumulative effects of water motion over time.

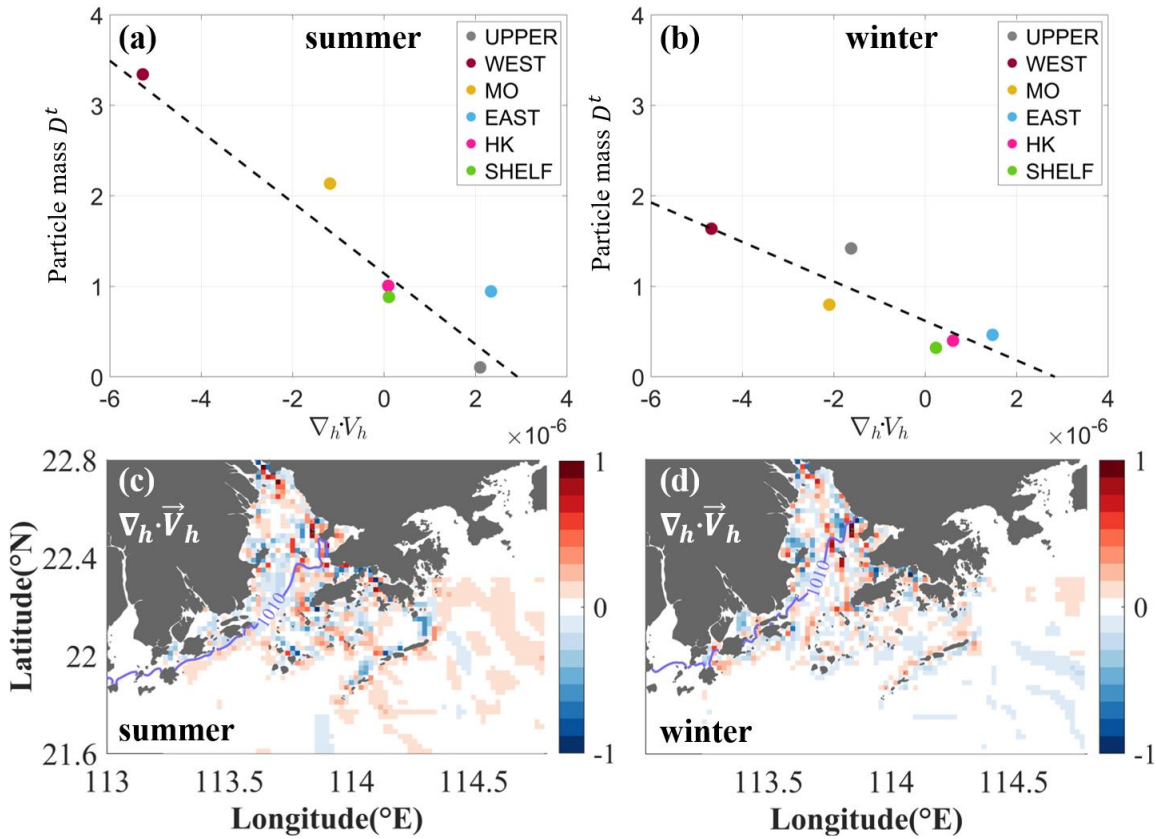


Figure 6: (a-b) Scatter plot of regional D^t against $\nabla_h \cdot \vec{V}_h$ for various subregions during summer and winter, respectively. (c-d) Horizontal distribution of $\nabla_h \cdot \vec{V}_h$ during summer and winter. The $\nabla_h \cdot \vec{V}_h$ is normalized by the largest divergence value in this area. Purple lines represented the isopycnic line of $1010 \text{ kg}\cdot\text{m}^{-3}$.

The existence of a salinity front acts as a barrier to particle transport and plays an important role in accumulation regions, such as coarse particles will accumulate at the bottom salinity front (Defontaine et al., 2020; He et al., 2018; Vermeiren et al., 2016). The coupling effect of velocity convergence and the front leads to particle accumulation in the middle estuary during winter and the lower estuary during summer (Malli, Corella-Puertas, Hajjar, & Boulay, 2022). In summer, the heightened river discharge creates the density front ($G = \sqrt{(\frac{\partial \rho}{\partial x})^2 + (\frac{\partial \rho}{\partial y})^2}$) (Fig. 7), affecting the particles transport and promoting their accumulation. The location of the front, roughly aligns with the outer boundary region of profound negative $\nabla_h \cdot \vec{V}_h$ over the WEST and MO region (Fig. 6c), further supporting the accumulation in these regions as the front hinders their offshore movement. During winter, the intrusion reaches the middle estuary, creating a blocking effect on the mass transport, which tends to remain confined to the upper part of the estuary (Lima, Barletta, & Costa, 2015; Lima, Costa, & Barletta, 2014). This retention likely contributes to the observed accumulation patterns, where the particles remain confined upstream owing to the blockage effect of the front. The $\nabla_h \cdot \vec{V}_h$ in winter also reflects this dynamic, with regions of negative values moving shoreward.

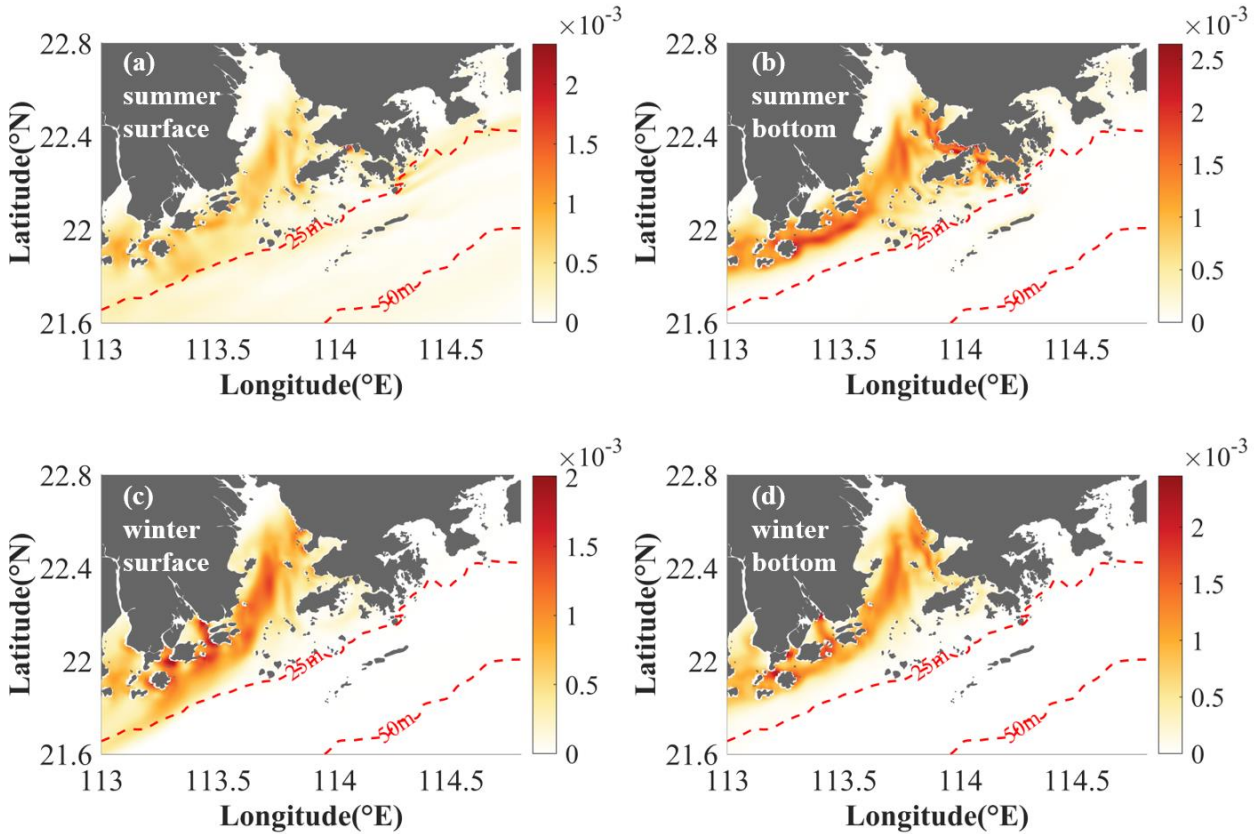


Figure 7: (a-b) The density front ($\text{kg}\cdot\text{m}^{-4}$) of the standard case at the surface layer and bottom layer in summer, respectively. (c-d) are the same as (a-b), but for winter.

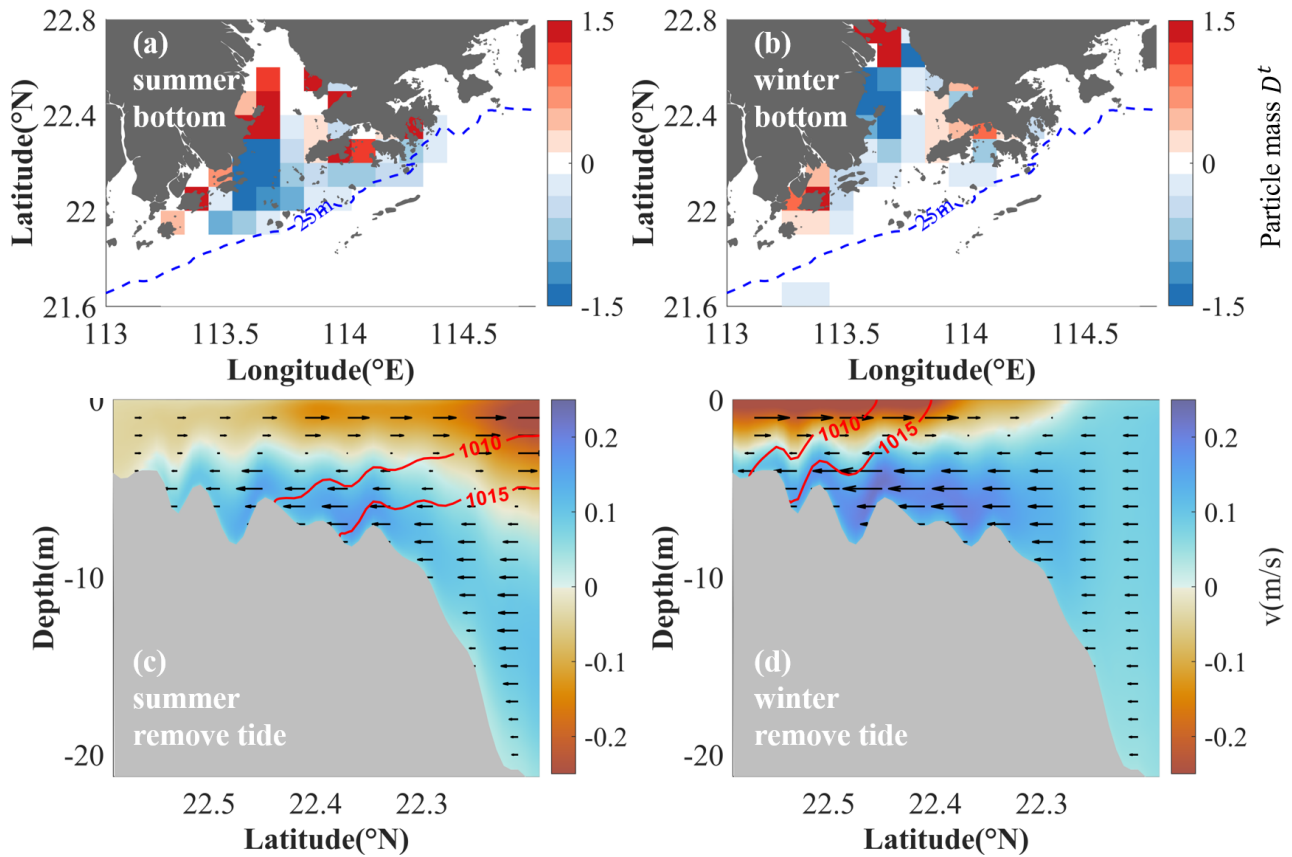
4 Discussion

265 The tides and rivers have essential influences on the estuarine circulation and associated mass transport in the PRE, whereas the wind mainly affects the shelf current and have less influence on the mass accumulation inside the estuary (figures not shown here). Two additional experiments are conducted to examine their contributions to the accumulation. In the case of reduced river discharge, the magnitude of river discharge in the forcing file is reduced by 20%. The magnitude of the tidal current is set to zero to remove the tidal currents. The accumulation regions and connections among the different regions
270 are investigated in the same way using the same Lagrangian tracking and analysis approach.

4.1 Tide

Because the tidal current affects the intensity of mixing in the water column, once removed, the offshore motion in the UPPER region is reduced during both summer and winter. The westward transport of Hong Kong water and adjacent shelf currents, flowing south of the WEST region, is strengthened in summer (Fig. S6a). In winter, the intrusion water from the
275 shelf moves directly landward and arrives at the upper part of the estuary. Along the transect of AB (Fig. S5b), we further examine the changes of the density stratification and vertical structure of circulation (Fig. 8c, d), revealing intensified and landward movement of the bottom intrusion associated with stronger density stratification. Removing tidal currents leads to weaker mixing and intensified stratification, as also revealed in previous studies where weaker tide intensity contributed to increased stratification in the PRE (e.g., Pan et al. (2020)).

280 *Anomaly of D^t between the case without tides and standard case, i.e., $D^t_{no-tide} - D^t_{standard}$ is compared in Figure 8.* Consequently, the removal of tidal forces intensifies particle accumulation in the middle of the WEST and northeastern parts of the EAST region during summer (Fig. 8a). Conversely, in the MO and HK regions, the absence of tides generally reduces the likelihood of accumulation, particularly in MO waters. In winter, the intensified onshore intrusion leads to higher accumulation in the UPPER regions (Fig. 8b). In contrast, in the WEST region, tides significantly hinder particles
285 from exiting the estuary because of the intensified landward motion of the westward transport shelf current, resulting in a negative accumulation anomaly when the tides are removed. Thus, the tidal current mainly resists bottom intrusion water in the midwestern estuary by changing the mixing intensity and density structure.



290 **Figure 8: (a-b) Particle mass (D^t) anomaly in the removing tide current case during summer and winter, respectively. A negative value represents the strengthened offshore transport without tidal current. (c-d) Without the tidal currents, the along transect velocity (color and arrow, positive indicate the onshore intrusion) and density contour of $1010 \text{ kg}\cdot\text{m}^{-3}$ and $1015 \text{ kg}\cdot\text{m}^{-3}$ (red lines) in AB during summer and winter, respectively.**

295 Same as the standard case, there is a negative correlation between the $\nabla_h \cdot \vec{V}_h$ and the particle mass D^t (Fig. 9a, b). The arrow represents the changes of $\nabla_h \cdot \vec{V}_h$ and particle mass due to the removal of tidal currents in the region, with significant changes in the particle mass. The decrease/increase in summer accumulation in the MO/EAST region correlates with the weakening or strengthening of the net convergence of the current due to the absence of the tidal current. Similarly, changes in winter accumulation in the UPPER, WEST, and EAST regions are also related to current divergence. However, it is

300 noteworthy that the WEST and MO regions where have relatively strong $\nabla_h \cdot \vec{V}_h$, the changes in accumulation are not significantly influenced by this divergence.

The impact of tides on water transport among the various identified subregions is investigated, as shown in Figure 9c-d. In summer, removing the tide resulted in strengthened attraction ability in the EAST and UPPER regions. The WEST region continues to exhibit a strong converging trend owing to the strengthened landward intrusion current, attracting particles

305 across the estuary. Notably, in the absence of tides, the MO region no longer converges particles from other regions.

Furthermore, particles originating from the EAST and UPPER regions ceased reaching the HK and MO regions. During winter, the UPPER region displays a heightened attraction to particles from the WEST, EAST, and MO regions, which is associated with intensified onshore currents from the lower estuary. The converging trend in the western region diminishes rapidly, reducing its role as a significant trap for water from other regions. There are no significant changes in EAST and
 310 HK, only MO traps more water from its own regions.

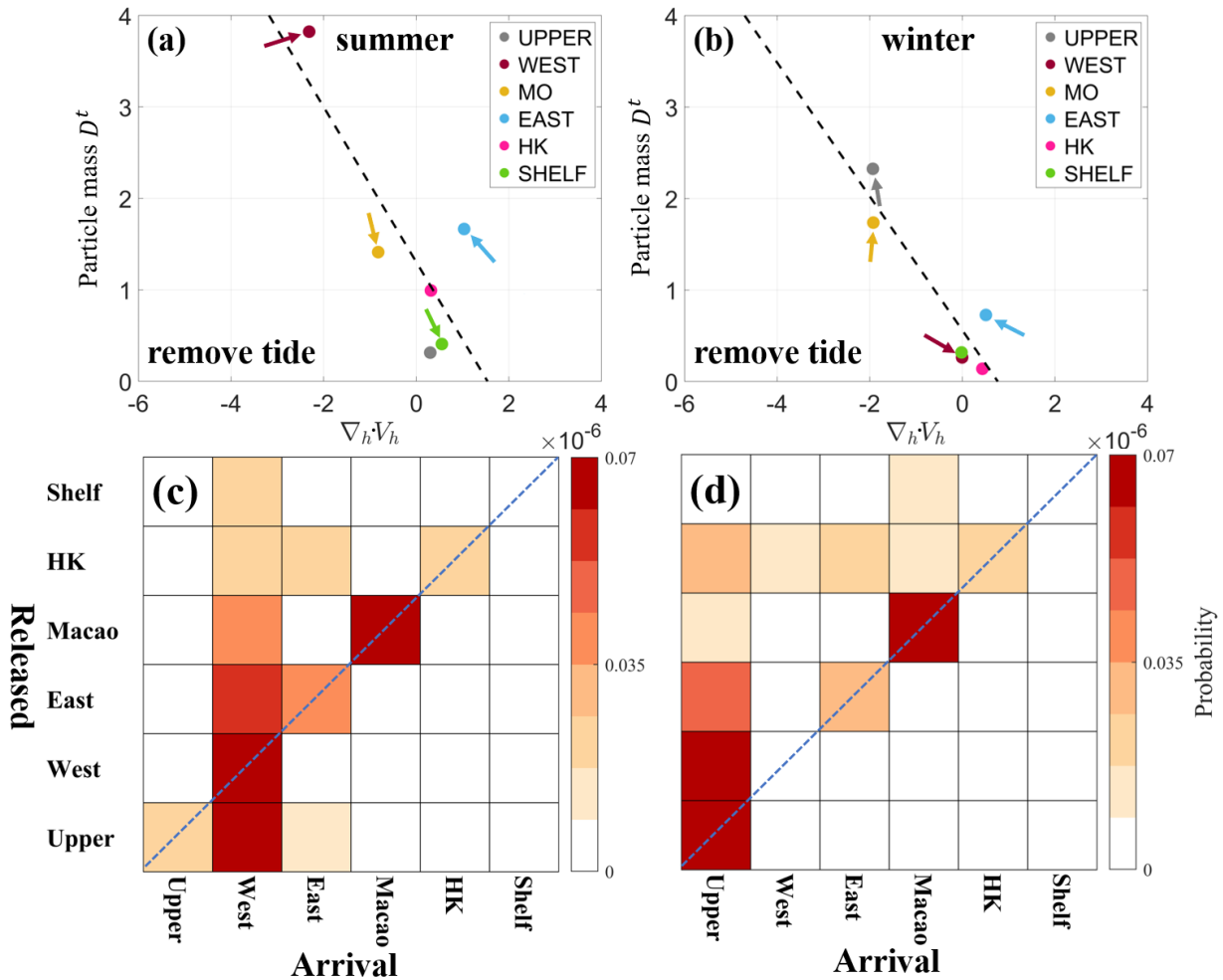


Figure 9: (a-b) Scatter plot of particle mass (D^t) against $\nabla_h \cdot \vec{V}_h$ for various subregions during summer and winter in removing tide cases. The arrow represents the changes of $\nabla_h \cdot \vec{V}_h$ and particle mass due to the removing of tide in each subregion. (c-d) The
 315 connection between six regions for removal of tidal current at the bottom layer during summer and winter time, respectively.

4.2 River discharge

Based on the circulation pattern of reduced river discharge, a significant decrease in seaward currents is observed in the entire estuary during both summer and winter (Fig. S6c, d). Similar with Figure 8, the anomaly results are calculated by
 320 using the D^t of case with reduced river discharges to subtract the D^t of the standard case (Fig. 10a, b). Along the AB

transect, the landward velocity increases in the upper estuary, while seaward motion accelerates in the lower estuary during winter (Fig. 10d), associated with the divergence and convergence of accumulation in the middle/lower estuary in winter (Fig. 10b). Increased landward currents have resulted in accumulation in the UPPER region. In summer, reduced stratification leads to a well-mixed water column in the inner estuary, and the landward movement of density to the middle estuary blocks the water in the upper part of the estuary (Fig. 10c). As a result, accumulation in the inner estuary increases in summer when river discharge is reduced (Fig.10b).

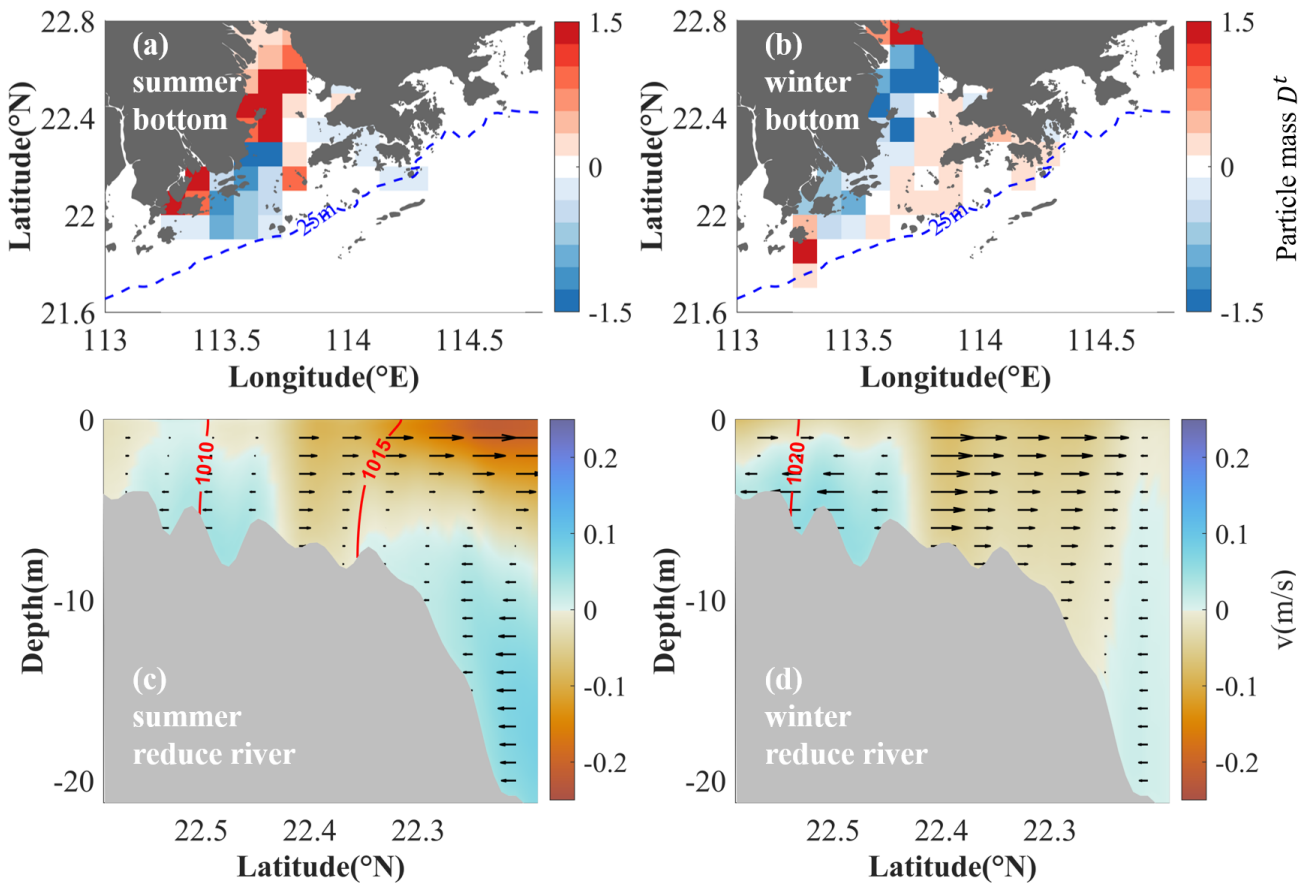


Figure 10: (a-b) Particle mass (D^t) anomaly in the reducing river discharge case during summer and winter, respectively. The negative value represents the strengthened offshore transport with fewer river discharges. (c-d) With reduced river discharge, the along transect velocity (color and arrow, positive indicate the onshore intrusion) and density contour of $1010 \text{ kg}\cdot\text{m}^{-3}$ and $1015 \text{ kg}\cdot\text{m}^{-3}$ (red lines) in AB during summer and winter, respectively.

Generally, major changes in regional accumulation are governed by the current convergence. In both seasons, variations in the net velocity convergence resulted in corresponding changes in particle mass in the UPPER, WEST, and EAST regions (Fig. 11a, b). Increased particle mass is accompanied by decreased net divergence.

Similarly, Fig. 11c-d illustrates that reduced river discharge greatly impacts the connections between the UPPER, WEST,

and MO regions. In summer, for the UPPER regions, the converging ability becomes stronger due to the rapidly reduced offshore currents and the blocking of the landward density front. Consequently, more particles from the UPPER remain in itself and no longer move to the EAST and MO regions. Moreover, reduced river discharge resulted in fewer particles from the MO region transporting into the WEST region. Instead, the EAST regions contribute more to the remain in the WEST regions. During winter, the interconnections among the six subregions are similar to those in the standard case (Fig. 5b). It should also be noted that the WEST regions converge fewer particles than the EAST and HK regions. Additionally, the MO regions attract particles from the WEST regions instead of from the SHELF.

345

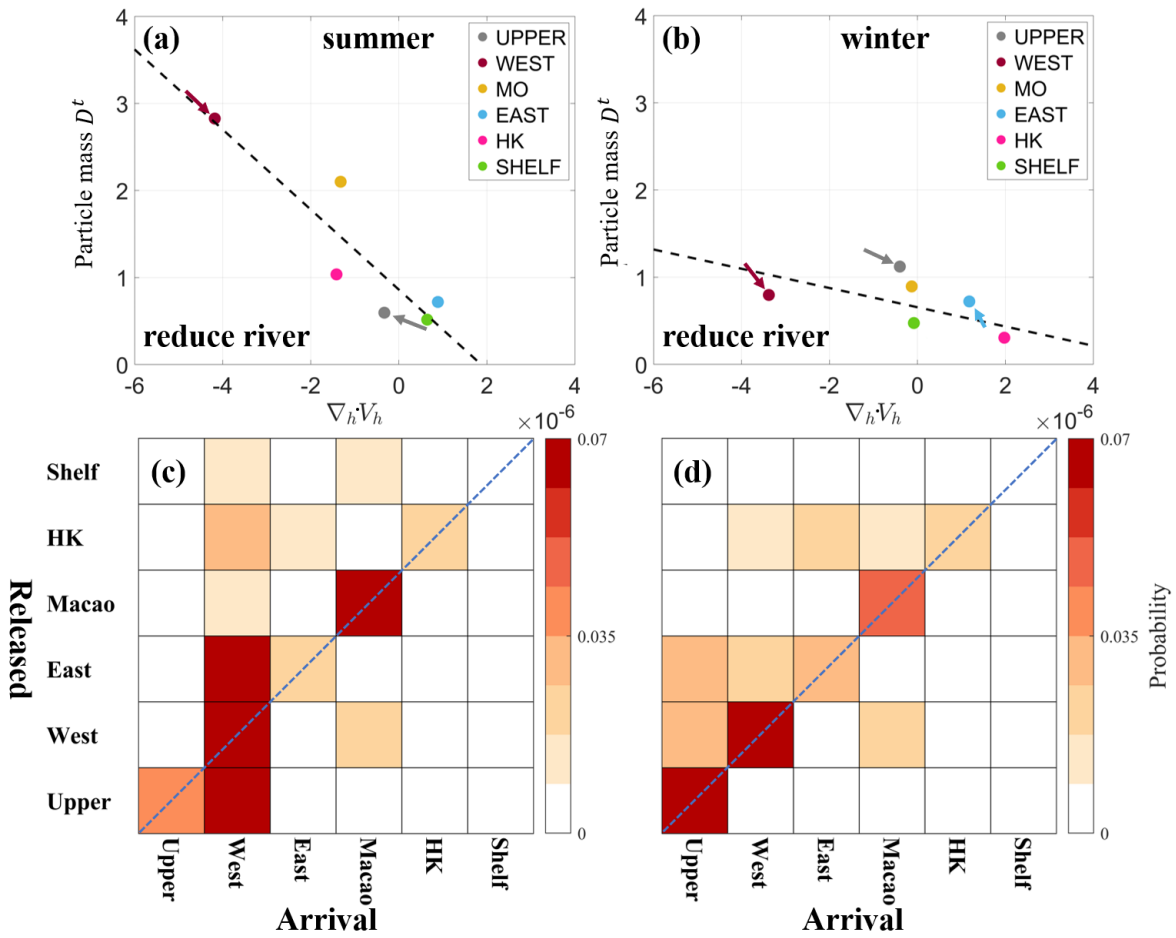


Figure 11: (a-b) Scatter plot of particle mass (D^t) against $\nabla_h \cdot \vec{V}_h$ for various subregions during summer and winter in river-reduced cases. The arrow represents the changes of $\nabla_h \cdot \vec{V}_h$ and particle mass due to the reduction of discharge in each subregion. (c-d) The connection between six regions for the case with reduced river discharge in summer and winter, respectively.

350

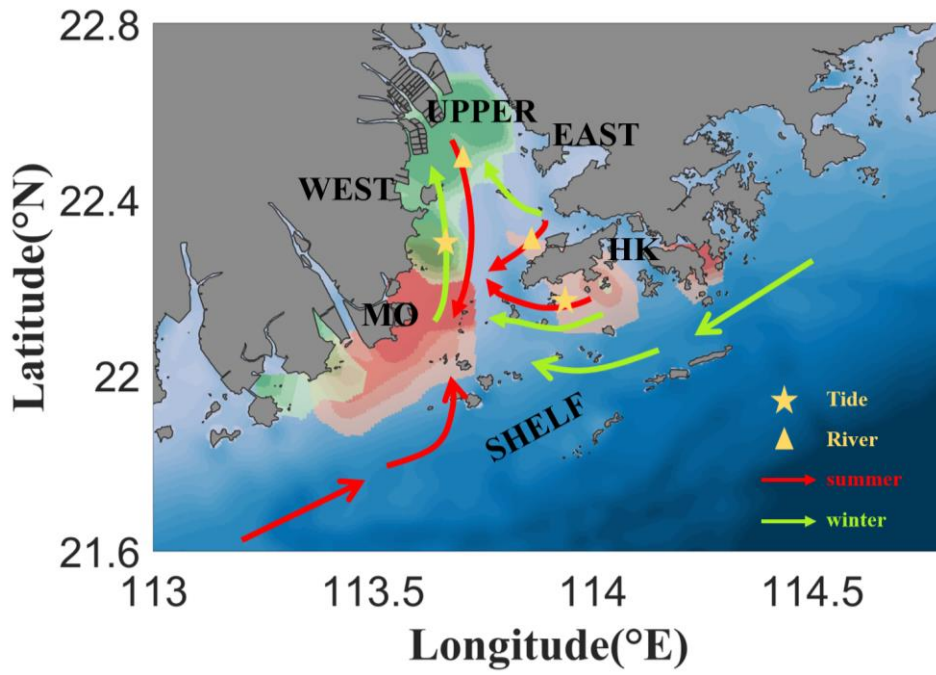
5 Conclusions

In this study, the Lagrangian method and Markov Chains were applied to illustrate the accumulation trends in different

PRE regions during typical monsoon seasons.

The accumulation patterns and regional connectivity are derived from the Markov Chains. Generally, surface offshore
355 transport is always quicker than that at the bottom owing to the strong offshore current and river discharge, leading to
relatively small accumulation at the surface layer. Conversely, significant accumulation occurs at the bottom, primarily in
the lower estuary during summer and moves shoreward during winter owing to the reduced river discharge and intensified
density front. Based on these bottom accumulation patterns, we identified six subregions in the PRE: UPPER, WEST,
EAST, MO, HK, and SHELF. Across these subregions, there is a negative correlation between the net divergence ($\nabla_h \cdot \vec{V}_h$)
360 and the accumulation, where intensified negative $\nabla_h \cdot \vec{V}_h$ provides favorable conditions for water accumulation.
Connections between the six subregions are discussed to illustrate the transport structure in the PRE. During summer,
regions like WEST and MO, characterized by substantial net negative divergence and strong fronts, act as powerful
accumulation targets that attract particles from almost the entire estuary. Conversely, EAST and HK waters show a
westward motion and are transported to the western estuary. In winter, accumulated regions display self-correlations, with
365 particles more likely to remain in their original regions. The UPPER region becomes a major accumulation area owing to
the blocking of the density front and the largely decreased river discharge. HK waters are transported throughout the entire
estuary, primarily contributing to the accumulation in the WEST regions under westward currents.

Sensitivity experiments are conducted to evaluate the impacts of tidal currents and river discharge on accumulation patterns.
Generally, tidal currents and river-induced gravitational circulation affect accumulation in different ways, affecting various
370 regions of the estuary. Their joint effects control the accumulation pattern. Tide currents enhance accumulation in the WEST
and UPPER regions during winter and in the MO and HK regions during summer through increased density stratification
and changes in water column mixing (Fig. 12). Increased river discharge is conducive to seaside transport in the UPPER
and WEST regions during summer and in the HK region during winter, associated with the intensified offshore current and
seaward movement of the density. Removal of tidal currents and reduced river discharges lead to intensified landward
375 current and westward transport current from HK waters and the adjacent shelf, accelerating bottom-water intrusion from
the lower estuary into the upper estuary.



380 Figure 12: The accumulation connections schematic in the PRE during summer (red arrow) and winter time (green arrow). The map color in red represents the high accumulations in summer, while green represented winter. The star indicates that the tide dominated the current, and the triangle represents river discharge.

Data availability

The corresponding authors can provide all raw data upon request.

385 **Author contributions**

M. L. conducted the investigation, methodology, and writing – original draft preparation; S. A. conducted the methodology and writing – review and editing; Z. C. conducted the conceptualization, supervision, and writing – review and editing; and T.Z. conducted the conceptualization and writing – review and editing.

Competing interests

390 The authors declare that they have no conflict of interest.

Acknowledgements

This work was supported by CORE, which is a joint research center for ocean research between the Laoshan Laboratory and HKUST. The simulation was performed at the SICCC, supported by SKL-IOTSC, University of Macau.

Financial support

395 This work was funded by the Science and Technology Development Fund, Macau SAR (0093/2020/A2, 001/2024/SKL), and the Open Research Project Program of the State Key Laboratory of the Internet of Things for Smart City (University of Macau) (Ref. No.: SKL-IoTSC(UM)-2021-2023/ORPF/A20/2022), National Natural Science Foundation of China (NSFC) under Project (42076026), Independent Research Project Program of the State Key Laboratory of Tropical Oceanography (LTOZZ2102), and General Research Fund (project ID 15216422) from the Research Grants Council of
400 Hong Kong.

References

- Acha, E. M., Mianzan, H. W., Guerrero, R. A., Favero, M., & Bava, J. (2004). Marine fronts at the continental shelves of austral South America: Physical and ecological processes. *Journal of marine systems*, *44*(1), 83-105. doi:10.1016/j.jmarsys.2003.09.005
- 405 Acha, E. M., Mianzan, H. W., Iribarne, O., Gagliardini, D. A., Lasta, C., & Daleo, P. (2003). The role of the Rio de la Plata bottom salinity front in accumulating debris. *Marine pollution bulletin*, *46*(2), 197-202. doi:[https://doi.org/10.1016/S0025-326X\(02\)00356-9](https://doi.org/10.1016/S0025-326X(02)00356-9)
- Ascione Kenov, I., Garcia, A. C., & Neves, R. (2012). Residence time of water in the Mondego estuary (Portugal). *Estuarine*,

- coastal and shelf science*, 106, 13-22. doi:10.1016/j.ecss.2012.04.008
- 410 Balachandran, K. K., Lalu Raj, C. M., Nair, M., Joseph, T., Sheeba, P., & Venugopal, P. (2005). Heavy metal accumulation in a flow restricted, tropical estuary. *Estuarine, coastal and shelf science*, 65(1), 361-370. doi:<https://doi.org/10.1016/j.ecss.2005.06.013>
- Banas, N. S., & Hickey, B. M. (2005). Mapping exchange and residence time in a model of Willapa Bay, Washington, a branching, macrotidal estuary. *Journal of Geophysical Research*, 110(C11), C11011-n/a. doi:10.1029/2005JC002950
- 415 Cai, Z., Liu, G., Liu, Z., & Gan, J. (2022). Spatiotemporal variability of water exchanges in the Pearl River Estuary by interactive multiscale currents. *Estuarine, coastal and shelf science*, 265, 107730. doi:10.1016/j.ecss.2021.107730
- Chenillat, F., Blanke, B., Grima, N., Franks, P. J. S., Capet, X., & Rivière, P. (2015). Quantifying tracer dynamics in moving fluids: a combined Eulerian-Lagrangian approach. 3. doi:10.3389/fenvs.2015.00043
- Chu, N., Liu, G., Xu, J., Yao, P., Du, Y., Liu, Z., & Cai, Z. (2022a). Hydrodynamical transport structure and lagrangian
- 420 connectivity of circulations in the Pearl River Estuary. 9. doi:10.3389/fmars.2022.996551
- Chu, N., Liu, G., Xu, J., Yao, P., Du, Y., Liu, Z., & Cai, Z. (2022b). Hydrodynamical transport structure and lagrangian connectivity of circulations in the Pearl River Estuary. *Frontiers in Marine Science*, 9. doi:10.3389/fmars.2022.996551
- Cui, L., Liu, Z., Chen, Y., & Cai, Z. (2024). Three-Dimensional Water Exchanges in the Shelf Circulation System of the Northern South China Sea Under Climatic Modulation From ENSO. *Journal of Geophysical Research: Oceans*, 129(4),
- 425 e2023JC020290. doi:<https://doi.org/10.1029/2023JC020290>
- Cui, Y., Wu, J., Ren, J., & Xu, J. (2019). Physical dynamics structures and oxygen budget of summer hypoxia in the Pearl River Estuary. *Limnology and Oceanography*, 64(1), 131-148. doi:<https://doi.org/10.1002/lno.11025>
- Dai, M., Guo, X., Zhai, W., Yuan, L., Wang, B., Wang, L., . . . Cai, W.-J. (2006). Oxygen depletion in the upper reach of the Pearl River estuary during a winter drought. *Marine chemistry*, 102(1), 159-169. doi:10.1016/j.marchem.2005.09.020
- 430 Dawson, M. N., Sen Gupta, A., & England, M. H. (2005). Coupled Biophysical Global Ocean Model and Molecular Genetic Analyses Identify Multiple Introductions of Cryptogenic Species. *Proceedings of the National Academy of Sciences - PNAS*, 102(34), 11968-11973. doi:10.1073/pnas.0503811102
- Defontaine, S., Sous, D., Tesan, J., Monperrus, M., Lenoble, V., & Lancelier, L. (2020). Microplastics in a salt-wedge estuary: Vertical structure and tidal dynamics. *Marine pollution bulletin*, 160, 111688.
- 435 doi:<https://doi.org/10.1016/j.marpolbul.2020.111688>
- Deng, Y., Liu, Z., Zu, T., Hu, J., Gan, J., Lin, Y., . . . Cai, Z. (2022). Climatic Controls on the Interannual Variability of Shelf Circulation in the Northern South China Sea. *Journal of Geophysical Research: Oceans*, 127(7), e2022JC018419. doi:<https://doi.org/10.1029/2022JC018419>
- Dippner, W. J. H. S. M. (2009). Mathematical modeling of the transport of pollution in water. 2, 204-246.
- 440 Dong, L., Su, J., Ah Wong, L., Cao, Z., & Chen, J.-C. (2004). Seasonal variation and dynamics of the Pearl River plume. *Continental shelf research*, 24(16), 1761-1777. doi:10.1016/j.csr.2004.06.006
- Drouin, K. L., & Lozier, M. S. (2019). The Surface Pathways of the South Atlantic: Revisiting the Cold and Warm Water Routes Using Observational Data. *Journal of geophysical research. Oceans*, 124(10), 7082-7103. doi:10.1029/2019JC015267
- 445 Drouin, K. L., Lozier, M. S., Beron-Vera, F. J., Miron, P., & Ollascoaga, M. J. (2022). Surface Pathways Connecting the South and North Atlantic Oceans. *Geophysical research letters*, 49(1), n/a. doi:10.1029/2021GL096646
- Fairall, C. W., Bradley, E. F., Hare, J., Grachev, A. A., & Edson, J. B. (2003). Bulk parameterization of air-sea fluxes: Updates and verification for the COARE algorithm. *Journal of climate*, 16(4), 571-591.
- Fok, L., & Cheung, P. K. (2015). Hong Kong at the Pearl River Estuary: A hotspot of microplastic pollution. *Marine*
- 450 *pollution bulletin*, 99(1), 112-118. doi:<https://doi.org/10.1016/j.marpolbul.2015.07.050>
- Gong, W., Shen, J., & Hong, B. (2009). The influence of wind on the water age in the tidal Rappahannock River. *Marine Environmental Research*, 68(4), 203-216. doi:<https://doi.org/10.1016/j.marenvres.2009.06.008>

- Harrison, P. J., Yin, K., Lee, J. H. W., Gan, J., & Liu, H. (2008). Physical–biological coupling in the Pearl River Estuary. *Continental shelf research*, 28(12), 1405-1415. doi:<https://doi.org/10.1016/j.csr.2007.02.011>
- 455 Haza, A. C., Özgökmen, T. M., & Hogan, P. (2016). Impact of submesoscales on surface material distribution in a gulf of Mexico mesoscale eddy. *Ocean modelling (Oxford)*, 107, 28-47. doi:10.1016/j.ocemod.2016.10.002
- He, C., Yin, Z.-Y., Stocchino, A., & Wai, O. W. H. (2023). Generation of macro-vortices in estuarine compound channels. *Frontiers in Marine Science*, 10. doi:10.3389/fmars.2023.1082506
- He, C., Yin, Z.-Y., Stocchino, A., Wai, O. W. H., & Li, S. (2022). The coastal macro-vortices dynamics in Hong Kong
460 waters and its impact on water quality. *Ocean Modelling*, 175, 102034. doi:<https://doi.org/10.1016/j.ocemod.2022.102034>
- He, Q., Zhan, H., Cai, S., He, Y., Huang, G., & Zhan, W. (2018). A New Assessment of Mesoscale Eddies in the South China Sea: Surface Features, Three-Dimensional Structures, and Thermohaline Transports. 123(7), 4906-4929. doi:<https://doi.org/10.1029/2018JC014054>
- Hinojosa, I. A., Rivadeneira, M. M., & Thiel, M. (2011). Temporal and spatial distribution of floating objects in coastal
465 waters of central–southern Chile and Patagonian fjords. *Continental shelf research*, 31(3), 172-186. doi:10.1016/j.csr.2010.04.013
- Jalón-Rojas, I., Wang, X. H., & Fredj, E. (2019). Technical note: On the importance of a three-dimensional approach for modelling the transport of neustic microplastics. *Ocean Sci.*, 15(3), 717-724. doi:10.5194/os-15-717-2019
- Jönsson, B. F., & Watson, J. R. (2016). The timescales of global surface-ocean connectivity. *Nature communications*, 7(1),
470 11239-11239. doi:10.1038/ncomms11239
- Lam, T. W. L., Fok, L., Lin, L., Xie, Q., Li, H.-X., Xu, X.-R., & Yeung, L. C. (2020). Spatial variation of floatable plastic debris and microplastics in the Pearl River Estuary, South China. *Marine pollution bulletin*, 158, 111383. doi:<https://doi.org/10.1016/j.marpolbul.2020.111383>
- Lane, R. R., Day, J. W., Marx, B. D., Reyes, E., Hyfield, E., & Day, J. N. (2007). The effects of riverine discharge on
475 temperature, salinity, suspended sediment and chlorophyll a in a Mississippi delta estuary measured using a flow-through system. *Estuarine, coastal and shelf science*, 74(1), 145-154. doi:<https://doi.org/10.1016/j.ecss.2007.04.008>
- Lebreton, L. C. M., Greer, S. D., & Borrero, J. C. (2012). Numerical modelling of floating debris in the world's oceans. *Marine pollution bulletin*, 64(3), 653-661. doi:<https://doi.org/10.1016/j.marpolbul.2011.10.027>
- Li, D., Gan, J., Hui, C., Yu, L., Liu, Z., Lu, Z., . . . Dai, M. (2021). Spatiotemporal Development and Dissipation of Hypoxia
480 Induced by Variable Wind-Driven Shelf Circulation off the Pearl River Estuary: Observational and Modeling Studies. 126(2), e2020JC016700. doi:<https://doi.org/10.1029/2020JC016700>
- Li, T., & Li, T.-J. (2018). Sediment transport processes in the Pearl River Estuary as revealed by grain-size end-member modeling and sediment trend analysis. *Geo-Marine Letters*, 38(2), 167-178. doi:10.1007/s00367-017-0518-2
- Li, X., Lu, C., Zhang, Y., Zhao, H., Wang, J., Liu, H., & Yin, K. (2020). Low dissolved oxygen in the Pearl River estuary
485 in summer: Long-term spatio-temporal patterns, trends, and regulating factors. *Marine pollution bulletin*, 151, 110814-110814. doi:10.1016/j.marpolbul.2019.110814
- Liang, J.-H., Liu, J., Benfield, M., Justic, D., Holstein, D., Liu, B., . . . Dong, W. (2021). Including the effects of subsurface currents on buoyant particles in Lagrangian particle tracking models: Model development and its application to the study of riverborne plastics over the Louisiana/Texas shelf. *Ocean modelling (Oxford)*, 167, 101879.
490 doi:10.1016/j.ocemod.2021.101879
- Lima, A. R. A., Barletta, M., & Costa, M. F. (2015). Seasonal distribution and interactions between plankton and microplastics in a tropical estuary. *Estuarine Coastal and Shelf Science*, 165, 213-225. doi:10.1016/j.ecss.2015.05.018
- Lima, A. R. A., Costa, M. F., & Barletta, M. (2014). Distribution patterns of microplastics within the plankton of a tropical estuary. *Environmental research*, 132, 146-155. doi:10.1016/j.envres.2014.03.031
- 495 Liu, Z., Zu, T., & Gan, J. (2020). Dynamics of cross-shelf water exchanges off Pearl River Estuary in summer. *Progress in Oceanography*, 189, 102465. doi:<https://doi.org/10.1016/j.pocean.2020.102465>

- Malli, A., Corella-Puertas, E., Hajjar, C., & Boulay, A.-M. (2022). Transport mechanisms and fate of microplastics in estuarine compartments: A review. *Marine pollution bulletin*, 177, 113553-113553. doi:10.1016/j.marpolbul.2022.113553
- 500 Mao, Q., Shi, P., Yin, K., Gan, J., & Qi, Y. (2004). Tides and tidal currents in the Pearl River Estuary. *Continental shelf research*, 24(16), 1797-1808. doi:10.1016/j.csr.2004.06.008
- Mellor, G. L., & Yamada, T. (1982). Development of a turbulence closure model for geophysical fluid problems. *Reviews of Geophysics*, 20(4), 851-875. doi:<https://doi.org/10.1029/RG020i004p00851>
- Mestres, M., Sánchez-Arcilla, A., Sierra, J. P., Mösso, C., Tagliani, P., Möller, O., & Niencheski, L. (2006). Coastal bays as a sink for pollutants and sediment. *Journal of Coastal Research*, 1546-1550.
- 505 Miron, P., Beron-Vera, F. J., Helfmann, L., & Koltai, P. (2021). Transition paths of marine debris and the stability of the garbage patches. *Chaos (Woodbury, N.Y.)*, 31(3), 033101-033101. doi:10.1063/5.0030535
- Miron, P., Beron-Vera, F. J., Olascoaga, M. J., Froyland, G., Pérez-Brunius, P., & Sheinbaum, J. (2019). Lagrangian Geography of the Deep Gulf of Mexico. *Journal of physical oceanography*, 49(1), 269-290. doi:10.1175/JPO-D-18-0073.1
- 510 Miron, P., Beron-Vera, F. J., Olascoaga, M. J., Sheinbaum, J., Pérez-Brunius, P., & Froyland, G. (2017). Lagrangian dynamical geography of the Gulf of Mexico. *Scientific reports*, 7(1), 7021-7021. doi:10.1038/s41598-017-07177-w
- North, E. W., Adams, E. E. E., Schlag, Z. Z., Sherwood, C. R., He, R. R., Hyun, K. H. K., . . . Enterprise, M. t. D. H. O. S. A. R. B. (2011). Simulating oil droplet dispersal from the Deepwater Horizon spill with a Lagrangian approach. 195, 217-226.
- North, E. W., Hood, R. R., Chao, S. Y., & Sanford, L. P. (2006). Using a random displacement model to simulate turbulent particle motion in a baroclinic frontal zone: A new implementation scheme and model performance tests. *Journal of marine systems*, 60(3), 365-380. doi:10.1016/j.jmarsys.2005.08.003
- 515 Pan, J., Lai, W., & Thomas Devlin, A. (2020). Circulations in the Pearl River Estuary: Observation and Modeling. In *Estuaries and Coastal Zones - Dynamics and Response to Environmental Changes*.
- Paris, C. B., Hénaff, M. L., Aman, Z. M., Subramaniam, A., Helgers, J., Wang, D.-P., . . . Srinivasan, A. (2012). Evolution of the Macondo Well Blowout: Simulating the Effects of the Circulation and Synthetic Dispersants on the Subsea Oil Transport. *Environmental Science & Technology*, 46(24), 13293-13302. doi:10.1021/es303197h
- 520 Shchepetkin, A. F., & McWilliams, J. C. (2005). The regional oceanic modeling system (ROMS): a split-explicit, free-surface, topography-following-coordinate oceanic model. *Ocean modelling (Oxford)*, 9(4), 347-404. doi:10.1016/j.ocemod.2004.08.002
- 525 Shen, P., Wei, S., Shi, H., Gao, L., & Zhou, W.-H. (2023). Coastal Flood Risk and Smart Resilience Evaluation under a Changing Climate. *Ocean-Land-Atmosphere Research*, 2, 0029. doi:doi:10.34133/olar.0029
- Song, Y., & Haidvogel, D. (1994). A Semi-implicit Ocean Circulation Model Using a Generalized Topography-Following Coordinate System. *Journal of Computational Physics*, 115(1), 228-244. doi:<https://doi.org/10.1006/jcph.1994.1189>
- 530 Tao, W., Niu, L., Dong, Y., Fu, T., & Lou, Q. (2021). Nutrient Pollution and Its Dynamic Source-Sink Pattern in the Pearl River Estuary (South China). *Frontiers in Marine Science*, 8. doi:10.3389/fmars.2021.713907
- van Sebille, E., Griffies, S. M., Abernathey, R., Adams, T. P., Berloff, P., Biastoch, A., . . . Zika, J. D. (2018). Lagrangian ocean analysis: Fundamentals and practices. *Ocean modelling (Oxford)*, 121(C), 49-75. doi:10.1016/j.ocemod.2017.11.008
- Vermeiren, P., Muñoz, C. C., & Ikejima, K. (2016). Sources and sinks of plastic debris in estuaries: A conceptual model integrating biological, physical and chemical distribution mechanisms. *Marine pollution bulletin*, 113(1-2), 7-16.
- 535 doi:10.1016/j.marpolbul.2016.10.002
- Wang, A.-j., Kawser, A., Xu, Y.-h., Ye, X., Rani, S., & Chen, K.-l. (2016). Heavy metal accumulation during the last 30 years in the Karnaphuli River estuary, Chittagong, Bangladesh. *SpringerPlus*, 5(1), 2079. doi:10.1186/s40064-016-3749-1
- 540 Wang, T., Zhao, S., Zhu, L., McWilliams, J. C., Galgani, L., Amin, R. M., . . . Chen, M. (2022). Accumulation, transformation and transport of microplastics in estuarine fronts. *Nature Reviews Earth & Environment*, 3(11), 795-805.

doi:10.1038/s43017-022-00349-x

Wong, L. A., Chen, J. C., Xue, H., Dong, L. X., Su, J. L., & Heinke, G. (2003). A model study of the circulation in the Pearl River Estuary (PRE) and its adjacent coastal waters: 1. Simulations and comparison with observations. *Journal of Geophysical Research: Oceans*, 108(C5). doi:<https://doi.org/10.1029/2002JC001451>

545 Ye, F., Huang, X., Zhang, D., Tian, L., & Zeng, Y. (2012). Distribution of heavy metals in sediments of the Pearl River Estuary, Southern China: Implications for sources and historical changes. *Journal of Environmental Sciences*, 24(4), 579-588. doi:[https://doi.org/10.1016/S1001-0742\(11\)60783-3](https://doi.org/10.1016/S1001-0742(11)60783-3)

Zhang, D., Zhang, X., Tian, L., Ye, F., Huang, X., Zeng, Y., & Fan, M. (2013). Seasonal and spatial dynamics of trace elements in water and sediment from Pearl River Estuary, South China. *Environmental Earth Sciences*, 68(4), 1053-1063.

550 doi:10.1007/s12665-012-1807-8

Zhang, H., & Li, S. (2010). Effects of physical and biochemical processes on the dissolved oxygen budget for the Pearl River Estuary during summer. *Journal of marine systems*, 79(1), 65-88. doi:<https://doi.org/10.1016/j.jmarsys.2009.07.002>

Zhang, L., Yin, K., Wang, L., Chen, F., Zhang, D., & Yang, Y. (2009). The sources and accumulation rate of sedimentary organic matter in the Pearl River Estuary and adjacent coastal area, Southern China. *Estuarine, coastal and shelf science*, 555 85(2), 190-196. doi:<https://doi.org/10.1016/j.ecss.2009.07.035>

Zhong, L., & Li, M. (2006). Tidal energy fluxes and dissipation in the Chesapeake Bay. *Continental shelf research*, 26(6), 752-770. doi:<https://doi.org/10.1016/j.csr.2006.02.006>

Zu, T., & Gan, J. (2015). A numerical study of coupled estuary–shelf circulation around the Pearl River Estuary during summer: Responses to variable winds, tides and river discharge. *Deep Sea Research Part II: Topical Studies in Oceanography*, 117, 53-64. doi:<https://doi.org/10.1016/j.dsr2.2013.12.010>

560 Zu, T., Gan, J., & Erofeeva, S. Y. (2008). Numerical study of the tide and tidal dynamics in the South China Sea. *Deep Sea Research Part I: Oceanographic Research Papers*, 55(2), 137-154. doi:<https://doi.org/10.1016/j.dsr.2007.10.007>

Zu, T., Wang, D., Gan, J., & Guan, W. (2014). On the role of wind and tide in generating variability of Pearl River plume during summer in a coupled wide estuary and shelf system. *Journal of marine systems*, 136, 65-79.

565 doi:<https://doi.org/10.1016/j.jmarsys.2014.03.005>